ATLAS CONF Note

ATLAS-CONF-2019-006

March 18, 2019

Search for long-lived, massive particles in events with a displaced vertex and a displaced muon in pp collisions at $\sqrt{s} = 13$ TeV with the ATLAS detector

The ATLAS Collaboration

A search for long-lived particles decaying into at least one muon and hadrons is presented. The analysis selects events that pass a muon or missing-transverse-momentum trigger and contain a displaced muon and a displaced vertex with at least three tracks and a visible invariant vertex mass of at least 20 GeV. The analyzed dataset of proton–proton collisions at $\sqrt{s} = 13$ TeV was collected with the ATLAS detector and corresponds to 136 fb^{-1}. The search employs dedicated reconstruction techniques that significantly increase the sensitivity to long-lived particle decays. Background estimates for Standard Model processes and instrumental effects are extracted entirely from data. The observed event yields are compatible with those expected from background processes. The results are presented as limits at 95% confidence level on model-independent cross sections for processes beyond the Standard Model, and interpreted as exclusion limits on scenarios with pair-production of long-lived top squarks that decay via a small R-parity-violating coupling to a quark and a muon. Top squarks with masses up to 1.7 TeV are excluded for a lifetime of 0.1 ns, and masses below 1.3 TeV are excluded for all lifetimes between 0.01 ns and 30 ns.

ATLAS-CONF-2019-006
21 March 2019

1 Introduction

The Standard Model of particle physics (SM) has successfully predicted the results of decades of laboratory experiments with impressive precision, but it suffers from several notable inadequacies. For example, the scale hierarchy of the interactions [1, 2] and dark matter [3] lack explanations in the SM, and it does not include a quantum description of gravity. However, despite ambitious search programs, the experiments at the Large Hadron Collider (LHC) have not yet reported any discoveries of physics beyond the Standard Model (BSM).

A possible way for BSM signatures to evade the constraints from these searches is for the BSM particles produced in proton–proton collisions to not decay promptly but have lifetimes sufficiently long to yield decay lengths of the order of 1 mm or more. Such long-lived particles (LLPs) can generate a variety of unconventional detector signatures that often completely lack irreducible backgrounds from SM processes. However, without dedicated reconstruction algorithms and analysis techniques that consider this possibility, a discovery of LLPs would likely be missed at today's facilities [4]. While there is a long history of searches for LLP signatures at colliders, such searches have attracted increased interest since the startup of the LHC [5]. This document reports a search for decays of LLPs including a muon using the full Run-2 dataset of the ATLAS experiment.

Extensions of the Standard Model involving Supersymmetry (SUSY) [6–11] are appealing from a theory perspective due to their potential to alleviate the naturalness problem [12–15]. Scenarios with a SUSY partner of the top quark, the *top squark* $\tilde{t}$, with a mass close to the weak scale are of particular interest. This is due to the role of the $\tilde{t}$ in the quadratic corrections to the Higgs mass that are at the center of the naturalness problem [16, 17].

The vast majority of searches for the $\tilde{t}$ have assumed that R-parity is conserved. This quantity is defined as $R_p \equiv (-1)^{3(B-L)+2s}$ where B, L, and s denote baryon number, lepton number, and spin, respectively. Apart from small nonperturbative effects [18, 19], B and L are conserved in the SM. It is often assumed that their conservation will translate to the SUSY sector to automatically avoid low-energy constraints on B- and L-violation. However, these conserved quantities in the SM are not due to fundamental symmetries, but are rather due to accidental symmmetries. In the minimally supersymmetric extension to the SM (MSSM) [20, 21], couplings that violate baryon-number and lepton-number conservation naturally occur at tree level. The couplings responsible for these violations are collectively called R-parity violating (RPV) couplings. The RPV terms of the MSSM superpotential are given by

$$\mathcal{W}_{\text{RPV}} = \mu_i l_i h_u + \lambda_{ijk} l_i l_j \bar{e}_k + \lambda'_{ijk} l_i q_j \bar{d}_k + \lambda''_{ijk} \bar{u}_i \bar{d}_j \bar{d}_k, \tag{1}$$

where μ_i, λ_{ijk}, λ'_{ijk}, and λ''_{ijk} are the RPV couplings, l and e represent the lepton and charged-lepton supermultiplets, and q, u, and d represent the quark, up-type quark, and down-type quark supermultiplets, respectively [22]. The symbols i, j, and k are generation indices. Non-zero RPV couplings can, for example, result in an unstable lightest SUSY particle (LSP) rendering constraints from many SUSY searches invalid. In such models, the LSP does not serve as a convenient dark matter candidate as it often does in R_p-conserving models [23, 24].

The search presented here targets nonzero values of the λ'_{ijk} coupling. All other RPV couplings are assumed to be exactly zero. Various low- and intermediate-energy constraints set upper limits on the size of these λ'_{ijk} couplings, particularly for couplings involving light flavors, such as measurements of the elements of the Cabibbo–Kobayashi–Maskawa matrix, constraints on neutrinoless double-beta decay, and B-physics

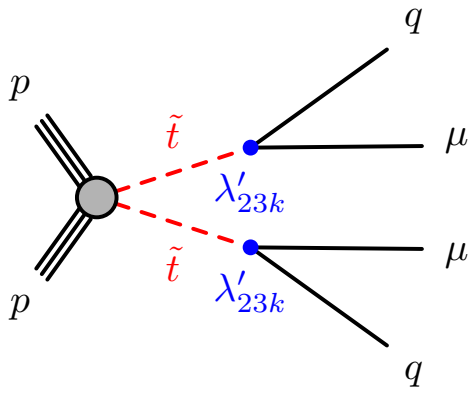

Figure 1: Diagram showing production of the top squark and its antiparticle (both denoted by $\tilde{t}$), in which the top squarks decay into a muon and a quark. With sufficiently small values of the R-parity-violating coupling λ'_{23k}, the lifetime of the $\tilde{t}$ becomes long enough to give rise to decays which are significantly displaced from their production point.

measurements. Many of these constraints suggest that the value of any non-zero RPV coupling needs to be small. In turn, this naturally leads to suppression of the decay processes and gives rise to long-lived SUSY particles. A non-zero λ'_{23k} coupling would allow a top squark to decay to a muon and a k^{th}-generation down-type quark, as shown in Figure 1. The strongest indirect constraints on this coupling come from partial width measurements of the Z boson at LEP excluding $\lambda'_{23k} > 0.45$ assuming the existence of a squark with a mass of 100 GeV. See Ref. [25] for a summary of experimental constraints on RPV SUSY.

In models with sufficiently small λ'_{23k} coupling values and where the $\tilde{t}$ is the LSP, the suppression of the decay causes it to occur at discernible distances from the pp interaction point where the $\tilde{t}$ pair was produced. This would give rise to muons and hadronic jets that are significantly displaced from the interaction point, yielding a distinctive detector signature in a collider experiment, with no irreducible backgrounds from SM processes. The search presented here is designed to be sensitive to this signature.

Other proposed BSM scenarios that could result in long-lived particle decays to at least one muon include long-lived lepto-quarks [26], long-lived BSM particles appearing in decays of Higgs bosons [27, 28], scenarios with right-handed neutrinos with Majorana masses below the electroweak scale [29] and RPV scenarios with a long-lived electroweakino LSP decaying through a virtual scalar muon and a λ'_{2jk} coupling [30].

Searches for a $\tilde{t}$ decaying promptly via the λ'_{ijk} couplings have been performed by the ATLAS and CMS collaborations [31, 32]. Exclusion limits on long-lived top squarks decaying to a muon and a hadronic jet have also been obtained by the CMS collaboration, excluding $\tilde{t}$ masses below 1.4 TeV for a mean proper lifetime of 0.1 ns [33–35]. Related searches for displaced lepton production in association with displaced hadronic activity have been performed by the ATLAS Collaboration [36, 37].

After a brief introduction of the ATLAS detector in Section 2, details of the analyzed dataset and the event reconstruction techniques are shown in Sections 3 and 4, respectively. The selection of events, estimation of background process yields, and various sources of uncertainties are described in Sections 5–7. Finally, the results and conclusions are presented in Sections 8 and 9.

2 ATLAS detector

The ATLAS detector [38] at the LHC is a multi-purpose particle detector with a forward-backward symmetric cylindrical geometry and a near 4π coverage in solid angle[1]. It consists of an Inner Detector (ID) surrounded by a thin superconducting solenoid, electromagnetic and hadronic calorimeters, and a Muon Spectrometer (MS) incorporating three large superconducting toroidal magnets.

The Inner Detector is immersed in a 2 T axial magnetic field and provides charged-particle tracking in the range $|\eta| < 2.5$. The high-granularity silicon Pixel detector covers the vertex region and typically provides four measurements per track, the first hit being normally in the insertable B-layer [39] located just outside the beam pipe at a radius of 33 mm from the proton beam line. Three more concentric pixel layers are situated at radii of 50.5 mm, 88.5 mm and 122.5 mm before the first active layer of the Semiconductor Tracker (SCT) at $r = 299$ mm. Based on silicon microstrip technology, the SCT typically provides eight separate measurements. These silicon detectors are complemented by the Transition Radiation Tracker (TRT), a straw-tube drift chamber which enables radially extended track reconstruction up to $|\eta| = 2.0$.

In the central pseudorapidity range, energy measurements are provided by a lead/liquid-argon (LAr) sampling calorimeter for electromagnetic deposits with high granularity, and a steel/scintillator-tile calorimeter for hadrons ($|\eta| < 1.475$ and $|\eta| < 1.7$, respectively). The end-cap and forward regions are instrumented with LAr calorimeters for both electromagnetic and hadronic energy measurements up to $|\eta| = 4.9$.

The Muon Spectrometer surrounds the calorimeters and is based on three large air-core toroidal superconducting magnets with eight coils each. The field integral of the toroids ranges between 2 and 6 T m across most of the detector. The MS includes a system of precision tracking chambers and fast detectors for triggering.

Interesting events are selected to be recorded by the first-level trigger system implemented in custom hardware, followed by selections made by algorithms implemented in software in the high-level trigger [40]. The first-level trigger reduces the 40 MHz bunch crossing rate to below 100 kHz, which the high-level trigger further reduces in order to record events to disk at about 1 kHz.

3 Data samples and simulated events

This analysis is performed on a set of proton–proton collision data at $\sqrt{s} = 13$ TeV recorded during 2016–2018 which, after requiring good quality of the data, corresponds to an integrated luminosity of 136 fb^{-1}. The relative uncertainty in the integrated luminosity is 1.7%. The LUCID-2 detector [41] is used for the baseline luminosity measurements, and the calibration and uncertainty determination was performed following a methodology using x–y beam-separation scans similar to that detailed in Ref. [42]. The data analyzed for this result were recorded using triggers requiring either a track in the MS with $p_{\mathrm{T}} > 60$ GeV and $|\eta| < 1.05$, or large missing transverse momentum $E_{\mathrm{T}}^{\mathrm{miss}}$ as measured in the calorimeters (100 GeV for

[1] ATLAS uses a right-handed coordinate system with its origin at the nominal interaction point (IP) in the center of the detector and the z-axis along the beam pipe. The x-axis points from the IP to the center of the LHC ring, and the y-axis points upwards. Cylindrical coordinates (r, ϕ) are used in the transverse plane, ϕ being the azimuthal angle around the z-axis. The pseudorapidity is defined in terms of the polar angle θ as $\eta = -\ln\tan(\theta/2)$. Angular distance is measured in units of $\Delta R \equiv \sqrt{(\Delta\eta)^2 + (\Delta\phi)^2}$.

a portion of the 2016 data, and 110 GeV for the rest of the analyzed dataset). In the recorded events, there are approximately 35 pp collisions in the same LHC bunch crossing, on average.

Samples of long-lived top squark–anti-squark pairs (denoted $\tilde{t}\bar{\tilde{t}}$) from Monte Carlo (MC) simulations are used as benchmarks to study expected signal efficiencies. Samples with 1 TeV $\leq m(\tilde{t}) \leq$ 2 TeV were generated in steps of 100 GeV, for mean proper lifetimes $\tau(\tilde{t})$ of 0.01, 0.1 and 1 ns for each mass value. All other SUSY-particle contributions are assumed to be decoupled. The matrix element calculation for the $\tilde{t}$ pair-production was performed to leading-order precision with MadGraph5_aMC@NLO 2.6.1 [43] with up to two additional outgoing partons, while the parton shower modeling was performed by Pythia 8.230 [44] with the A14 set of tuned parameters [45] for the modeling of the parton showering, hadronization and underlying event. Parton distribution functions (PDF) from the NNPDF23LO [46] set were used. In the signal models considered in this document, the $\tilde{t}$ lifetime is larger than the hadronization timescale in quantum chromodynamics (QCD). Since the $\tilde{t}$ carries color charge, it will undergo a hadronization process in Pythia and form a composite color-singlet state with SM quarks, an *R-hadron*. Dedicated routines for hadronization of heavy colored particles [22] were used to simulate the hadronization process. The top squarks primarily form meson-like states ($\tilde{t}\bar{q}$), but approximately 10% of them form baryon-like states ($\tilde{t}qq$). Roughly half of the *R*-hadrons formed around the top squarks have nonzero electric charge, and due to the $\tilde{t}\bar{\tilde{t}}$ production the two *R*-hadrons cannot have same-sign charge.

The *R*-hadron from Pythia is then propagated through a simulated model of the ATLAS detector [47] implemented in Geant 4 v10.1.3 [48] employing dedicated models for *R*-hadron interactions with the detector material [49–51] that can alter the content of the light-quark system in the *R*-hadron, possibly changing its electric charge as it traverses the detector. At the position of the decay, the *R*-hadron is passed to an instance of Pythia which simulates the decay to final-state particles using a parton shower model. The resulting decay products are then further propagated through the detector simulation, originating from the point of the *R*-hadron decay. The decay process $\tilde{t} \to \mu b$ is simulated although nonzero b-lifetime effects are not considered. Because of this, results are interpreted in a decay model $\tilde{t} \to \mu j$.

Signal production cross sections are calculated to approximate next-to-next-to-leading order in the strong coupling constant, adding the resummation of soft gluon emission at next-to-next-to-leading-logarithmic accuracy (approximate NNLO+NNLL) [52–55]. The nominal cross sections and their uncertainties are derived using the PDF4LHC15_mc PDF set, following the recommendations of Ref. [56].

Samples of $Z \to \mu^+\mu^-$ events generated using Powheg v1 r2856 [57] and Pythia 8.186 [44] reconstructed with the same configuration as the signal samples (See Section 4) are used to determine scale factors accounting for small differences in muon identification efficiency between the data and the MC simulation.

All simulated event samples include the effects of pileup, i.e. multiple pp interactions per bunch crossing as well as effects on the detector response due to activity from bunch crossings before or after the one containing the selected event.

4 Special event reconstruction

The standard ATLAS track reconstruction is optimized for the trajectories of charged particles originating from the interaction region, or from decays of short-lived particles such as b-hadrons. To reduce the computational complexity, constraints are therefore placed on the transverse and longitudinal impact parameters of track candidates with respect to the interaction region ($|d_0| < 10$ mm and $|z_0| < 250$ mm, respectively). In order to reconstruct tracks from the decays of long-lived BSM particles, which typically

have impact parameters which fall outside the standard constraints, a dedicated track reconstruction is performed using *large-radius tracking* (LRT) [58]. The LRT uses hits not already associated with tracks reconstructed by the standard tracking algorithm in order to improve the efficiency for tracks not originating from the interaction region. Requirements on the track impact parameters are relaxed to $|d_0| < 300$ mm and $|z_0| < 1500$ mm. Requirements on the number of hits which are allowed to be shared by multiple tracks are also relaxed. Tracks from the standard processing and the LRT processing are treated as a single collection in all subsequent steps of reconstruction, such as in the reconstruction of muons used in this search.

A dedicated secondary-vertex reconstruction algorithm for LLP decays is employed to reconstruct displaced vertices (DVs). As input to this vertex reconstruction, only tracks with transverse momentum $p_{\mathrm{T}} > 1$ GeV and $|d_0| > 2$ mm are considered. The requirement placed on the track transverse impact parameter ensures most tracks associated with the primary vertex (PV), or the point at which a proton-proton interaction occurred, and those from decays of short-lived, lower-mass SM particles such as b-hadrons, are ignored in vertex reconstruction. In order to avoid contamination of the vertex reconstruction with fake tracks, which are reconstructed from spurious combinations of hits, the input-track selection includes several additional requirements. Tracks are required to have at least six SCT hits or at least one Pixel hit. A track is rejected if it both has fewer than two pixel hits and completely lacks TRT hits. Tracks with $p_{\mathrm{T}} < 25$ GeV are subject to the additional requirements of having at least seven SCT hits, as well as having at least 20 TRT hits if within $|\eta| < 1.6$. Since only tracks with $|d_0| > 2$ mm are considered, a track from a charged LLP originating at the PV will not be included in the vertex reconstructed from its decay products.

The DV reconstruction begins by finding all possible two-track seed vertices from all possible pairs of selected tracks. The seed vertices are required to have a fit with χ^2 per degree of freedom less than 5. Several additional requirements are then applied to ensure the seed vertex is consistent with the decay of a particle originating from the PV. Firstly, both tracks of the seed vertex are required to not have hits in pixel layers at radii smaller than the position of the seed vertex, and are required to have a hit in the first pixel or SCT layer at larger radius. If a seed vertex is inside or within several millimeters of a tracker barrel layer, hits in that particular layer are neither forbidden nor required. This avoids penalizing cases in which it is unclear on which side of the layer the vertex is. Secondly, the direction of the vector sum of the momenta of the tracks associated to the seed vertex is required to be consistent with the vector pointing from the primary to the secondary vertex.

The collection of all possible two-track seed vertices is then iteratively merged to form n-track vertices. Ambiguities for tracks compatible with more than one vertex are resolved based on comparing their χ^2 in the vertex fit, or by merging the vertices if the distance between their estimated positions is not significant enough. To recover losses due to the tight requirements on the tracks used in the seed-vertex finding, tracks compatible with the reconstructed vertices are also attached even if they have associated hits in lower-radius layers. Extra requirements are made on the impact parameter transverse to the beam axis for the tracks before attaching them to the DV in order to suppress fake tracks from the reconstruction.

In the following, the number of associated tracks for a given vertex is denoted $n^{\mathrm{DV}}_{\mathrm{Tracks}}$, and its visible invariant mass calculated from the four-momenta of the associated tracks, assuming each track was produced by a charged pion, is denoted m_{DV}.

The missing transverse momentum $E^{\mathrm{miss}}_{\mathrm{T}}$ of an event is usually defined as the negative vector sum of the transverse momenta of all identified physics objects (electrons, photons, muons, jets) calibrated individually. In this analysis, an alternative definition using only topological clusters of energy deposits in the calorimeters is used instead. The clusters are locally calibrated to the hadronic scale, but no object-level

information is used to calibrate the clusters [59]. In the following this is referred to as *cluster-based* $E_{\mathrm{T}}^{\mathrm{miss}}$. This definition is used because of its similarity to the $E_{\mathrm{T}}^{\mathrm{miss}}$ definition which is used in the trigger system, which is based solely on energy deposits in the calorimeter. The benchmark signal considered in this analysis does not include any genuine missing transverse momentum, but since high-p_{T} muons are expected to only deposit a small fraction of their energy in the calorimeters through ionization, most of their momentum is unaccounted for making the $E_{\mathrm{T}}^{\mathrm{miss}}$ trigger efficient for this signature.

5 Event selection

As the LRT processing is computationally expensive, it cannot be run on all events recorded with the ATLAS detector. Instead, during the prompt processing of the data, a subset of the events are selected for a tightly filtered stream of raw data events. This stream is later processed using the special reconstruction configuration described in Section 4. This filtering is therefore the first step in this analysis, defining the start of two mutually exclusive trigger-based event selections:

- **$E_{\mathrm{T}}^{\mathrm{miss}}$-triggered sample:** Events recorded with the $E_{\mathrm{T}}^{\mathrm{miss}}$ trigger were required to have cluster-based $E_{\mathrm{T}}^{\mathrm{miss}} > 180$ GeV, in order to ensure events are close to the plateau of the turn-on curve of the $E_{\mathrm{T}}^{\mathrm{miss}}$ trigger. The $E_{\mathrm{T}}^{\mathrm{miss}}$ trigger threshold varied in the range $100 - 110$ GeV over the period in which the data were recorded.
- **Muon-triggered sample**: Events recorded with the muon trigger requiring a track in the MS with $|\eta| < 1.05$ are required to have at least one reconstructed muon with $p_{\mathrm{T}} > 60$ GeV and $|\eta| < 2.5$. Reconstructed muons are not required to be matched to the muon that fired the trigger in the filtering step, though a trigger matching requirement is made after events are processed with special reconstruction. For events recorded during 2016 data-taking, MS tracks that had a well-matched ID track were required to have $|d_0| > 1.5$ mm. For the events recorded during 2017–2018 data taking, no requirement on the muon d_0 was imposed. The cluster-based $E_{\mathrm{T}}^{\mathrm{miss}}$ is required to be less than 180 GeV in order to make the two samples mutually exclusive.

Events that survive the filtering step detailed above are subject to additional selection criteria. Muon candidates are required to be reconstructed in both the ID and the MS with $p_{\mathrm{T}} > 25$ GeV and $|\eta| < 2.5$. In order to reject muons that originate from SM particles, the d_0 of the muon with respect to the primary vertex is required to be larger than 2 mm. Additionally, muon $|d_0|$ and $|z_0|$ are required to be less than 300 mm. These requirements define the *muon preselection*.

Additional selection criteria are applied to preselected muons to reject major sources of background. The sources identified for large d_0 muons are from cosmic rays, reconstruction algorithm fakes, and muons from in-flight decays of SM hadrons, especially those containing heavy-flavor quarks.

To reduce the contribution of cosmic rays, events which have activity in the MS on the opposite side of the muon are rejected. The spatial positions of track segments reconstructed in individual muon stations are compared to the momentum of the reconstructed muon. Muons with matching segments on the opposite side of the MS that satisfy $|\eta(\text{muon momentum}) + \eta(\text{segment position})| < 0.05$ and $|\Delta\phi(\text{muon momentum, segment position}) - \pi| < 0.22$ are rejected. The asymmetry between the ϕ and η requirements is due to the MS detector geometry and its superior resolution in segment η. Track segments are used for this veto instead of fully reconstructed muon tracks which are more likely to fail to be reconstructed for muons not pointing back to the interaction region. Angular corrections are applied to

account for the longitudinal displacement of the muon. Muons are also rejected if they are back-to-back in η and in ϕ with a region of the MS without detector coverage. This requirement is designed to ensure that if the muon were to pass through the detector like a cosmic ray, it would pass through an instrumented region of the MS and can produce a track segment on the opposite side of the muon. Together, these requirements constitute the *cosmic-muon veto*.

Accidental reconstruction of fake displaced muons, from spurious combinations of hits, can also occur. Such fake muons, however, tend to have poor quality of fit and fewer hits on track. To reject these fake muon candidates, they are required to be constructed from segments in at least three MS stations and have a quality of fit $\chi^2/N_{\mathrm{DoF}} < 8$. The latter requirement is kept loose to avoid MS alignment mismodeling effects. These requirements constitute the *fake-muon veto*.

Muons produced in semileptonic decays of short-lived SM hadrons can also contribute to the background processes for this search. Primarily these are decays of hadrons containing heavy-flavor quarks. However, such muons are most often produced with nearby energy depositions from hadronic activity. As a result, such processes can be rejected by requiring that the muons be isolated from nearby ID tracks and calorimeter deposits. The sum of track p_{T} in a cone of varying size around the muon is required to be no more than 6% of the muon p_{T}. The cone has a maximum size of $\Delta R = 0.3$ for muons with $p_{\mathrm{T}} < 33.3$ GeV, and a cone size of 10 GeV/p_{T} is used for muons with higher p_{T}. Additionally, the sum of calorimeter cluster p_{T} in a cone of $\Delta R < 0.2$ around the muon is required to be no more than 6% of the muon p_{T}. These two requirements define the *heavy-flavor veto*.

Together, the cosmic-muon, fake-muon, and heavy-flavor veto criteria define the *full muon selection*.

DVs are required to be reconstructed in a cylindrical volume with radius $r_{\mathrm{DV}} < 300$ mm and longitudinal extent $|z_{\mathrm{DV}}| < 300$ mm, have a fit $\chi^2/N_{\mathrm{DoF}} < 5$, and have a transverse distance from all reconstructed PVs greater than 4 mm. To reject vertices arising due to interactions with dense detector material, DVs are further required to not have a position consistent with sensitive elements of the detector, its support structures or services. This veto is imposed via a three-dimensional map of detector material that is constructed from measured positions of low-mass vertices in an inclusive sample and the known positions of detector elements. These requirements define the *DV preselection*. DVs pass the *full DV selection* if they in addition satisfy $n^{\mathrm{DV}}_{\mathrm{Tracks}} \geq 3$ and $m_{\mathrm{DV}} > 20$ GeV, requirements designed to reduce the expected backgrounds to around one event.

Table 1 lists the preselection and full selection criteria for muons and DVs.

Selection level	**Muon selection**	**Displaced vertex selection**
Preselection	$p_{\mathrm{T}} > 25$ GeV, $\lvert\eta\rvert < 2.5$, 2 mm $< \lvert d_0\rvert < 300$ mm, $\lvert z_0\rvert < 500$ mm	$r_{\mathrm{DV}} < 300$ mm, $\lvert z_{\mathrm{DV}}\rvert < 300$ mm, $\min(\lvert\vec{r}_{\mathrm{DV}} - \vec{r}_{\mathrm{PV}}\rvert) > 4$ mm, $\chi^2/N_{\mathrm{DoF}} < 5$, Pass material map veto
Full selection	Pass cosmic-muon, fake-muon, and heavy-flavor vetoes	$n^{\mathrm{DV}}_{\mathrm{Tracks}} \geq 3$, $m_{\mathrm{DV}} > 20$ GeV

Table 1: Selection requirements for muons and displaced vertices

The *event preselection* is applied by requiring that events have at least one selected primary vertex with at least two tracks and $|z_{\mathrm{PV}}| < 200$ mm and at least one preselected muon. Events in the signal regions

(SRs) are required to have at least one fully selected muon and at least one fully selected DV, as described above. Two orthogonal SRs are defined based on the trigger used to record events. The *Muon Trigger SR* uses the MS track trigger described above and requires cluster-based $E_{\mathrm{T}}^{\mathrm{miss}}$ below 180 GeV and a muon with $p_{\mathrm{T}} > 62$ GeV and $|\eta| < 1.05$ to ensure efficient triggering. This muon is further required to spatially coincide with the trigger-level muon. The E_T^{miss} *Trigger SR* uses the $E_{\mathrm{T}}^{\mathrm{miss}}$-based trigger described above and requires that the cluster-based $E_{\mathrm{T}}^{\mathrm{miss}}$ be larger than 180 GeV. The event selection requirements are summarized in Table 2.

Selection level	$\boldsymbol{E_{\mathrm{T}}^{\mathrm{miss}}}$ **Trigger SR**	**Muon Trigger SR**
Preselection	Selected by $E_{\mathrm{T}}^{\mathrm{miss}}$ trigger, Cluster-based $E_{\mathrm{T}}^{\mathrm{miss}} > 180$ GeV, Selected PV, preselected muon,	Selected by muon trigger, Cluster-based $E_{\mathrm{T}}^{\mathrm{miss}} < 180$ GeV, Selected PV, preselected muon, Highest-p_{T} muon matches trigger muon
Full selection	≥ 1 full-selection muon, ≥ 1 full-selection DV	

Table 2: Event selection requirements

6 Background estimation

The backgrounds for displaced muons described in Section 5 are largely removed by dedicated veto requirements. Sources of background for DVs include material interactions and randomly intersecting tracks, which are efficiently suppressed by requiring $m_{\mathrm{DV}} > 20$ GeV and $n_{\mathrm{Tracks}}^{\mathrm{DV}} \geq 3$, respectively.

The background estimation used in this analysis relies on the fact that the variables used to reject displaced muons from background sources are uncorrelated with the variables used to reject displaced vertices from background. This is exploited in order to estimate backgrounds in the SR from data. The following subsections describe how the residual backgrounds from cosmic rays, algorithm fakes, and heavy-flavor decays in the SRs are determined.

6.1 Region definitions

Preselected events are divided into three regions depending on the DV properties:

- **DV Control Region (DV CR)**: no DVs passing the preselection, comprising three sub-regions:
  - No DVs with a good fit quality in the volume of interest,
  - Only two-track DVs failing the material map veto,
  - Only three-track DVs failing the material map veto;
- **DV Validation Region (DV VR)**: preselected DVs not passing the full selection, comprising two sub-regions:
  - Preselected two-track DVs,

  - Preselected DVs with $m_{\mathrm{DV}} < 20$ GeV and $n^{\mathrm{DV}}_{\mathrm{Tracks}} > 2$; and

- **DV Signal Region (DV SR)**: DVs passing the full selection.

For each muon background, a control region (CR) enriched with events of this background is defined by inverting the dedicated veto. A transfer factor is then determined as the ratio of the number of events passing the veto and the number of events rejected by it. As the probability of passing or failing the muon veto does not depend on the DV properties of the event, this transfer factor can be measured in the DV CR and applied in the DV SR in order to estimate the background contribution.

The following muon selections are used to define an orthogonal slicing of the dataset:

- **Fake-muon CR**: full muon selection with the fake-muon veto inverted,
- **Heavy-flavor CR**: full muon selection with the heavy-flavor veto inverted,
- **Cosmic-muon CR**: full muon selection with the cosmic-muon veto inverted, and
- **Muon SR**: full muon selection.

The final signal regions used in this search are the intersections of the DV SR requirements and the Muon SR requirements.

6.2 Transfer factor determination

The DV CR is used to determine the transfer factors for each of the three muon backgrounds. For background i, the transfer factor f_i is measured as

$$f_i = \frac{N(\text{Preselected events; DV} \in \text{DV CR; } \mu \textbf{ passes} \text{ veto } i \text{ and passes } \mathrm{d_0} \text{ selection } i)}{N(\text{Preselected events; DV} \in \text{DV CR; } \mu \textbf{ fails} \text{ veto } i \text{ and passes } \mathrm{d_0} \text{ selection } i)} \tag{2}$$

where events in both the numerator and denominator are required to pass the other two vetos that comprise the muon full-selection.

The fake-muon and heavy-flavor transfer factors are determined in the $E_{\mathrm{T}}^{\mathrm{miss}}$-triggered sample, but because a larger number of events with cosmic muons are expected to be found in the muon-triggered sample, the corresponding transfer factor is determined in those events. Additionally, to minimize the impact of muons from heavy-flavor decays on the determination of the transfer factors for fake-muon and cosmic-muon backgrounds, those are determined using preselected muons with 5 mm$< |d_0| <$ 300 mm. For similar reasons, the heavy-flavor transfer factor is measured using preselected muons with 1.5 mm $< |d_0| <$ 3.0 mm. Table 3 reports the transfer factors extracted from the data in the DV CR.

Background source (i)	**Transfer factor (f_i)**
Cosmic-ray muons	$(4.0 \pm 0.2\ (\text{stat.}) \pm 0.5\ (\text{syst.})) \times 10^{-3}$
Fake muons	$(1.0 \pm 0.3\ (\text{stat.}) \pm 0.5\ (\text{syst.})) \times 10^{-2}$
Heavy-flavor muons	$(9.1 \pm 1.6\ (\text{stat.}) \pm 4.0\ (\text{syst.})) \times 10^{-2}$

Table 3: Transfer factors used to calculate background estimates, extracted from control regions

Though fake-muon and heavy-flavor transfer factors are measured in the $E_{\mathrm{T}}^{\mathrm{miss}}$-triggered sample, they are also applied in the muon-triggered sample. The cosmic-ray transfer factor is similarly applied to the $E_{\mathrm{T}}^{\mathrm{miss}}$-triggered sample. In order to ensure the extrapolation between streams is safe, a separate measurement of the heavy-flavor transfer factor is made in the muon-triggered sample and compared to the nominal transfer factor. Agreement within uncertainties is observed. It is impossible to repeat this check with cosmic and fake-muon transfer factors, because they are negligible backgrounds in the $E_{\mathrm{T}}^{\mathrm{miss}}$-triggered and muon-triggered samples respectively. Furthermore, cosmic muons are expected to behave the same regardless of the trigger used to collect the event.

6.3 Background predictions

Using the transfer factors determined from the data, the background in the final SRs of the analysis can be predicted for each source i by multiplying the event yield observed in the corresponding muon CR, N_i^{CR}, in events with at least one DV passing the full selection (DV SR). The total expected background N_{SR} in each SR of the analysis is then given by

$$N_{SR} = \sum_i N_i^{\mathrm{CR}} \times f_i. \tag{3}$$

Similarly, the transfer factors are validated by comparing their predictions with the observed data in the DV VR to gain confidence that the method works. The VR is divided into two separate regions, one with two-track DVs and one with low-mass DVs with three tracks or more. The observed results of this validation are discussed in Section 8.

Using the technique described above, the total predicted background yields are 0.43 ± 0.16 (stat.) ± 0.16 (syst.) for the $E_{\mathrm{T}}^{\mathrm{miss}}$ Trigger SR and 1.88 ± 0.20 (stat.) ± 0.28 (syst.) for the Muon Trigger SR.

7 Uncertainties

Uncertainties affecting the estimated SR event yields for the various sources of background are assessed by using transfer factors extracted in sub-regions of the CRs, and taking the maximal difference with respect to the nominal transfer factor measurement. The DV CR is divided into three subregions of events: those with no reconstructed DV and those with two-track DVs or three-track DVs that do not pass the material veto. Uncertainties are also assessed by measuring transfer factors with varying requirements on the muon d_0. For the fake and cosmic-ray transfer factors, separate measurements are evaluated for muons with $5 < |d_0| < 100$ mm and $100 < |d_0| < 300$ mm. For the heavy flavor transfer factor, transfer factors are evaluated for muons with $1.5 < |d_0| < 1.7$ mm and $1.7 < |d_0| < 3$ mm. These impact parameter selections were designed to minimize the statistical uncertainties on the alternative transfer factor measurements. The uncertainties from these two variations are added in quadrature. The uncertainties for the final SR background predictions quoted in Section 6 are determined in this way.

A number of factors affect the uncertainty of the event yields predicted for signal scenarios, and this section outlines how their impact on the final selection efficiencies ϵ_{sel} is determined.

The largest overall uncertainty is related to the dedicated LRT and secondary-vertex reconstruction. The radial distributions of secondary vertices from K_s^0 decays are compared in data and MC simulation, after normalizing the two distributions by the number of vertices at low radii, where tracking efficiencies are well understood. The mismodeling of the reconstruction efficiency in MC at large track impact parameter and large vertex radius is estimated in this comparison. The largest observed discrepancy is applied as a conservative per-track efficiency uncertainty of ±10% which is then applied to the tracks associated with displaced vertices in the signal samples. The effect on final event counts with a fully selected DV is determined to be 15%.

By comparing the $E_{\mathrm{T}}^{\mathrm{miss}}$ trigger efficiency turn-on as function of cluster-based $E_{\mathrm{T}}^{\mathrm{miss}}$ in $Z \to \mu^+\mu^-$ events in data and MC simulation, an $E_{\mathrm{T}}^{\mathrm{miss}}$-dependent correction (between 0 and 10%) is extracted and applied to the MC samples for events which have cluster-based $E_{\mathrm{T}}^{\mathrm{miss}}$ between 180 and 220 GeV. The relative difference in the final SR event yield with and without this correction is taken as systematic uncertainty. The uncertainties on energy scale and resolution for the clusters calibrated to the hadronic energy scale entering the $E_{\mathrm{T}}^{\mathrm{miss}}$ calculation used in this search are assessed by applying systematic uncertainties for hadronic jets [60]. The same variations are also observed to have a small effect on the muon isolation efficiency. The combined effect is determined to be no more than 2.1% which is applied to all signal efficiencies.

For the efficiency of the MS-only muon trigger, the relative efficiency degradation as a function of d_0 with respect to prompt muons as measured in MC signal samples is taken as an uncertainty. The per-track efficiency uncertainty extracted above from K_s^0 decays is also applied for the ID part of the muon track. The muon reconstruction and selection criteria efficiency are also measured in MC signal samples, and the degradation as a function of d_0 with respect to prompt muons is taken as an uncertainty. The effects of these three uncertainties are assumed to be uncorrelated. Their combined impact on the signal SR yields are 10–12% for the signal samples. In addition, since custom muon identification criteria are applied, differences between data and MC are corrected for by comparing efficiencies for prompt muons in $Z \to \mu^+\mu^-$ events in data and MC samples processed with the special reconstruction used for the analysis. The statistical uncertainties of these measured scale factors are propagated to the final SR event yields for signal, resulting in an impact of 0.9–4.0% on the total selection efficiency.

To assess the sensitivity to effects due to imperfect modeling of the pileup interactions in the signal samples, a reweighting is applied to the MC signal samples to cover the uncertainty in the number of pp interactions in the data. The largest relative difference in ϵ_{sel} is determined to be between 0.37 and 2.2%. Another uncertainty stems from the modeling of initial-state QCD radiation which affects the kinematics of the $\tilde{t}\tilde{t}$ system and thus the cluster-based $E_{\mathrm{T}}^{\mathrm{miss}}$ and the muon p_{T} distribution. To assess the sensitivity of ϵ_{sel} to this, a reweighting of the p_{T} distribution of the $\tilde{t}\tilde{t}$ system in the MadGraph5_aMC@NLO events is applied to simulate that of Pythia 6.427. The resulting impact is 3%. Finally, the uncertainty in the integrated luminosity of the dataset of 1.7% is included as that translates directly to an uncertainty in the expected yield of signal events in the SRs.

The impact of the systematic uncertainties affecting ϵ_{sel} for signal events is summarized in Table 4.

8 Results

No events are observed in the $E_{\mathrm{T}}^{\mathrm{miss}}$ Trigger SR when 0.43 ± 0.16 (stat.) ± 0.16 (syst.) events are expected in the absence of signal, while a single event is observed in the Muon Trigger SR where

Source of uncertainty	Relative impact on ϵ_{sel} for signal events [%]
Total	18 – 20
Tracking and vertex reconstruction	15
Displaced muon efficiency	10 – 12
Prompt muon efficiency	(0.01 – 0.7) $\oplus$ (0.9 – 4.0)
Radiation modeling in MC simulation	3
Pileup modeling	0.37 – 2.2
Hadronic energy scale and resolution (affecting $E_{\text{T}}^{\text{miss}}$)	2.1
Integrated luminosity of dataset	1.7
$E_{\text{T}}^{\text{miss}}$ trigger efficiency	< 0.2

Table 4: Summary of impact of systematic uncertainties on event selection efficiency ϵ_{sel} for the signal scenarios with pair-produced long-lived top squarks

1.88 ± 0.20 (stat.) $\pm$ 0.28 (syst.) events are expected. The observed event yields are in good agreement with the background-only expectations.

Figure 2 shows the distributions of the variables used for the final two vertex-selection requirements in events with a muon passing the full muon selection. The track multiplicity $n_{\text{Tracks}}^{\text{DV}}$ is shown for all preselected displaced vertices. The invariant mass m_{DV} is shown for the highest-mass preselected displaced vertex with at least three associated tracks. The individual background predictions are derived from muon CR distributions scaled by the transfer factors described in Section 6.

For all four distributions, there is good agreement between the number of vertices observed in data and the background prediction. The DV full selection requirements, $n_{\text{Tracks}}^{\text{DV}} \geq 3$ and $m_{\text{DV}} > 20$ GeV are visualized with a black arrow. For the m_{DV} distributions, inverting the requirement denoted by the black arrow gives the low-mass DV VR, showing good agreement between the expected background normalization and the observed number of events.

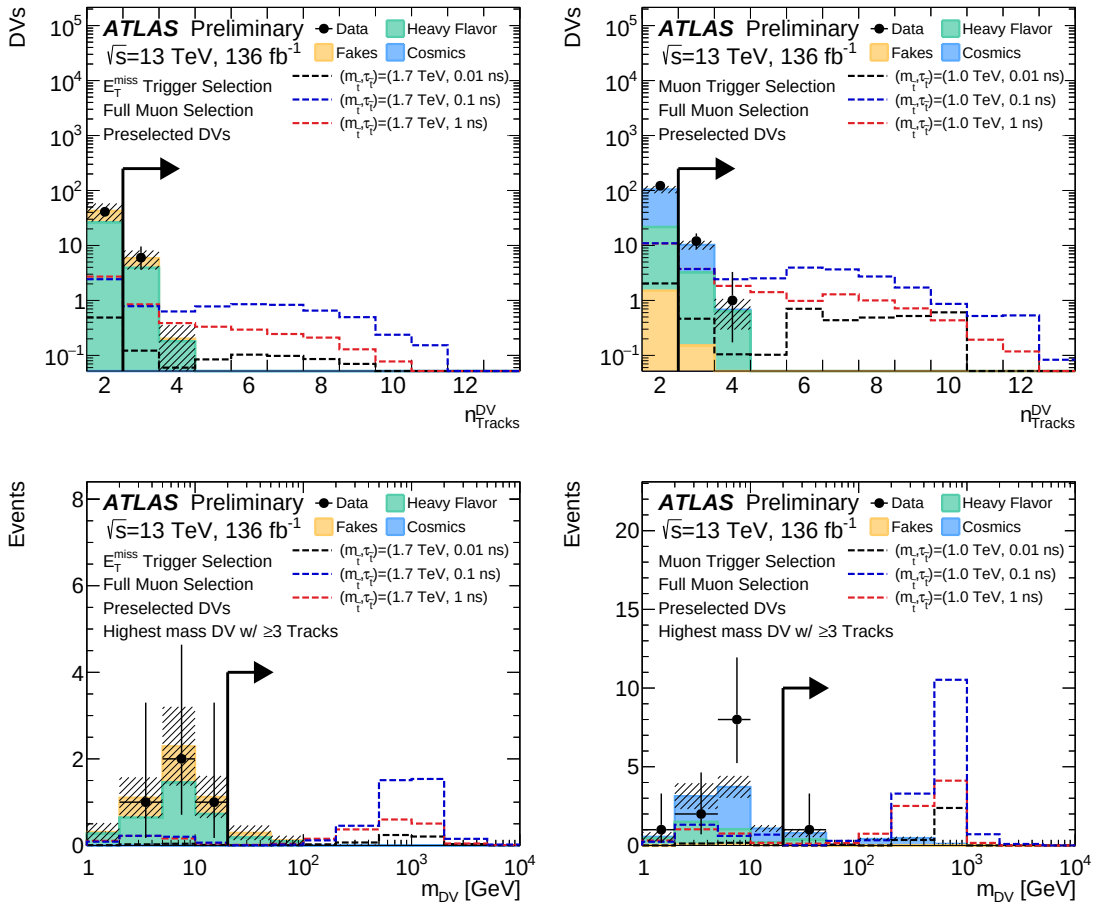

Figure 2: Track multiplicity $n^{\mathrm{DV}}_{\mathrm{Tracks}}$ (top) for preselected DVs and invariant mass m_{DV} (bottom) for the highest-mass preselected DV with at least three associated tracks in events with at least one muon passing the full selection, in the $E^{\mathrm{miss}}_{\mathrm{T}}$-triggered (left) and muon-triggered (right) samples. Along with the data shown with black markers, the stacked filled histograms represent the background estimates, and predictions for signal scenarios are overlaid with dashed lines. The errors include statistical and systematic uncertainties and are indicated by hatched bands. The DV full selection requirements, $n^{\mathrm{DV}}_{\mathrm{Tracks}} \geq 3$ and $m_{\mathrm{DV}} > 20$ GeV are visualized with a black arrow.

Signal and data event yields are shown as a function of progressively stricter requirements in Figure 3 along with the cumulative selection efficiencies. For the signal model considered here, over 95% of events have cluster-based $E^{\mathrm{miss}}_{\mathrm{T}}$, and the $E^{\mathrm{miss}}_{\mathrm{T}}$ trigger SR has the largest overall signal efficiency. For signals with $\tau(\tilde{t}) = 0.1$ ns, the total selection efficiency of the $E^{\mathrm{miss}}_{\mathrm{T}}$ trigger SR is 35%. Signals with $\tau(\tilde{t}) = 1$ ns have a total efficiency of 15%, due to the reduced efficiency for reconstructed displaced tracks and displaced vertices at large radii. Signals with $\tau(\tilde{t}) = 0.01$ ns have total selection efficiencies between 5–6%, because many stop decays ocurr within milimeters of the primary vertex. Signals with $\tau(\tilde{t}) = 0.01$ ns lose efficiency when requiring at least one muon with $|d_0| > 2$ mm, or a DV which is at least 4 mm away from any primary vertex in the event.

The final yields in the control, validation and signal regions are shown in Figure 4. In the DV CRs, good agreement is observed between data and prediction. Note that perfect agreement in not expected because

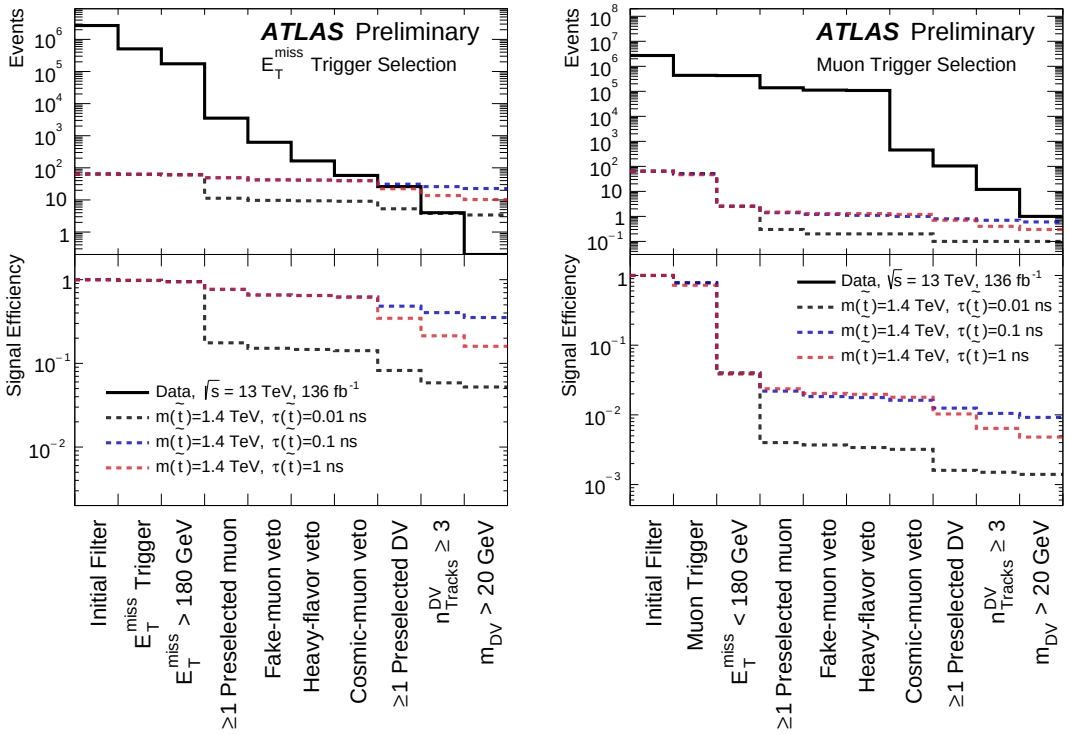

Figure 3: Event yields are shown as a function of the SR requirements for data and three example signal models for the $E_{\mathrm{T}}^{\mathrm{miss}}$ Trigger selection (left) and the Muon Trigger selection (right). The Initial Filter requirement includes selections on the data due to the raw event filters. The $E_{\mathrm{T}}^{\mathrm{miss}}$ requirement label denotes requirements on the cluster-based $E_{\mathrm{T}}^{\mathrm{miss}}$.

transfer factors are measured using muons with modified impact parameter requirements. In the DV VRs, the data show agreement with the background predictions within uncertainties, validating the assumptions made in the background estimation. In the SRs, the data show good agreement with the background predictions within uncertainties.

The HistFitter package [61] was used for the calculation of the 95% CL exclusion limits using the CL_s prescription [62]. Figure 5 shows expected and observed 95% CL exclusion limits on the mass of a long-lived $\tilde{t}$ as a function of its mean proper lifetime $\tau(\tilde{t})$. The sensitivity to the shown region of parameter space comes primarily from the $E_{\mathrm{T}}^{\mathrm{miss}}$ Trigger SR. Additionally, in Figure 5, 95% CL upper limits on the production cross section of these signals are shown as a function of $m(\tilde{t})$ for various values of $\tau(\tilde{t})$.

Contours showing fixed values of $\lambda'_{23k} \cos\theta_t$ are also shown in Figure 5 where θ_t is the mixing angle between the left- and right-handed $\tilde{t}$ squarks. These contours are derived using the parametrization provided in Ref. [5] for a $\tilde{t}$ decay via a single λ'_{ijk} coupling:

$$\tau(\tilde{t}) \sim \left(\frac{500\ \mathrm{GeV}}{m(\tilde{t})}\right)\left(\frac{10^{-7}}{\lambda'_{23k}}\right)^2\left(\frac{0.12}{\cos^2\theta_t}\right) \times 10^{-3}\ \ \mathrm{ns}. \tag{4}$$

For a mean proper lifetime of $\tau(\tilde{t}) = 0.1$ ns, masses below roughly $m(\tilde{t}) = 1.7$ TeV are excluded. For the wide range of mean proper lifetime values between 0.01 ns and 30 ns, masses below 1.3 TeV are excluded

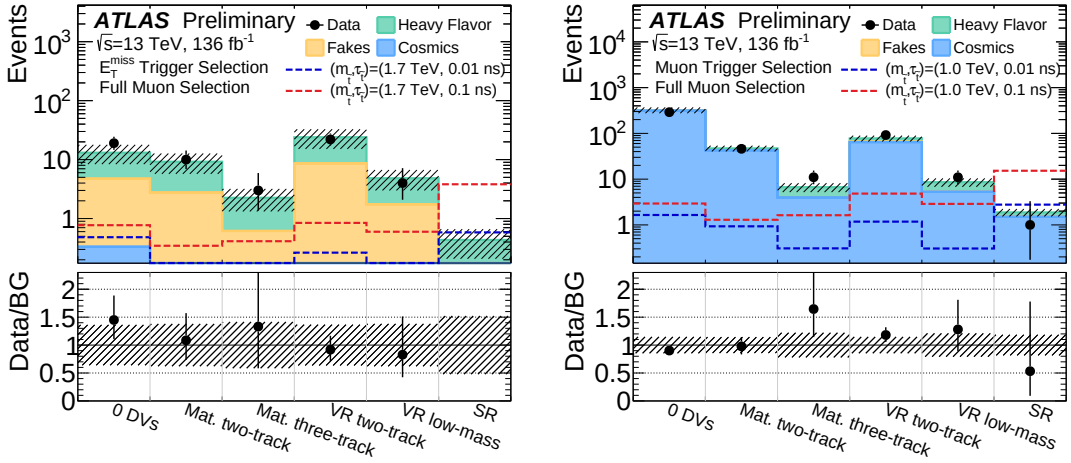

Figure 4: The observed event yields in the control, validation and signal regions are shown for the $E_{\mathrm{T}}^{\mathrm{miss}}$ Trigger (left) and Muon Trigger (right) selections, along with the predicted background yields. The bottom panel shows the ratio of observed events to the total background yields. The errors represent the total uncertainty of the backgrounds prediction, including the statistical and systematic uncertainties added in quadrature.

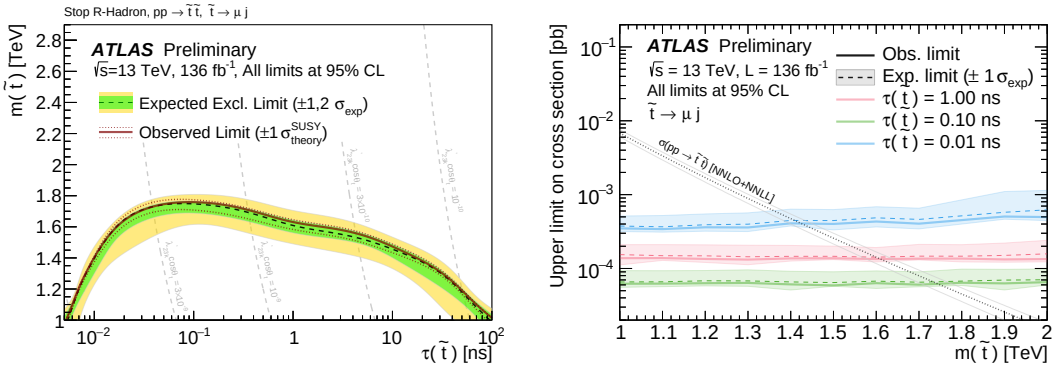

Figure 5: Exclusion limits at 95% CL on $m(\tilde{t})$ as a function of $\tau(\tilde{t})$ are shown (left) along with contours showing fixed values of $\lambda'_{23k}\cos\theta_t$. Experimental and theoretical uncertainties are shown. Limits on the production cross section as a function of $m(\tilde{t})$ for several values of $\tau(\tilde{t})$ are also shown along with the nominal signal production cross section and its theoretical uncertainty (right).

at 95% CL. For $\tau(\tilde{t}) = 0.1$ ns, cross section upper limits are set below 100 ab. For mean proper lifetimes between 0.01 ns and 100 ns, these limits are the strictest to date on models with a metastable $\tilde{t}$ decaying via the λ'_{ijk} RPV coupling. For $m(\tilde{t}) = 1$ TeV, values of $\lambda'_{23k}\cos\theta_t$ between roughly 10^{-8} and 10^{-10} are excluded at 95% CL.

Model-independent upper limits at 95% CL on the number of BSM events in the signal region are also derived, neglecting any significant contamination in the control regions. Normalizing these limits by the integrated luminosity of the data sample, these numbers can be interpreted as upper limits on the visible BSM cross section, denoted σ_{vis}. It is defined as the product of signal acceptance, reconstruction efficiency, and production cross section. The results are given in Table 5.

Signal Region	S^{95}_{obs}	S^{95}_{exp}	$\langle\sigma_{\text{vis}}\rangle^{95}_{\text{obs}}$[fb]
$E_{\text{T}}^{\text{miss}}$ Trigger SR	3.1	$3.1^{+1.1}_{-0.1}$	0.023
Muon Trigger SR	3.7	$4.2^{+1.6}_{-1.0}$	0.027

Table 5: The observed 95% CL upper limits on the visible cross section $\langle\sigma_{\text{vis}}\rangle^{95}_{\text{obs}}$, and the observed ($S^{95}_{\text{obs}}$) and expected ($S^{95}_{\text{exp}}$) limits on the number of signal events.

9 Conclusion

A search for physics beyond the Standard Model giving rise to long-lived particle decays with muons is performed with the ATLAS experiment using 136 fb^{-1} of pp collision data at $\sqrt{s}$ = 13 TeV. Event selections are developed to efficiently reject backgrounds. The yields expected in the signal regions from background are extracted from control regions in the data and amount to 0.43 ± 0.16 (stat.) ± 0.16 (syst.) in the $E_{\text{T}}^{\text{miss}}$ Trigger SR, and 1.88 ± 0.20 (stat.) ± 0.28 (syst.) in the Muon Trigger SR. The data agree with the yields expected from the background-only hypothesis, with zero and one events passing the $E_{\text{T}}^{\text{miss}}$ and Muon Trigger SR requirements, respectively.

The results are interpreted in a supersymmetric model with pair-produced top squarks $\tilde{t}$ decaying via small values of the R-parity violating coupling λ'_{23k} to a muon and a quark, giving the $\tilde{t}$ mean proper lifetimes $\tau(\tilde{t})$ in the ps to ns range. At 95% CL, $m(\tilde{t})$ values up to 1.7 TeV for $\tau(\tilde{t})$ = 0.1 ns are excluded, and the limit surpasses 1.3 TeV for all lifetimes in the range from 0.01 ns to 30 ns. Upper limits on the visible cross section for physics with the sought signature are 0.023 fb and 0.027 fb for the $E_{\text{T}}^{\text{miss}}$ and Muon Trigger SRs, respectively.

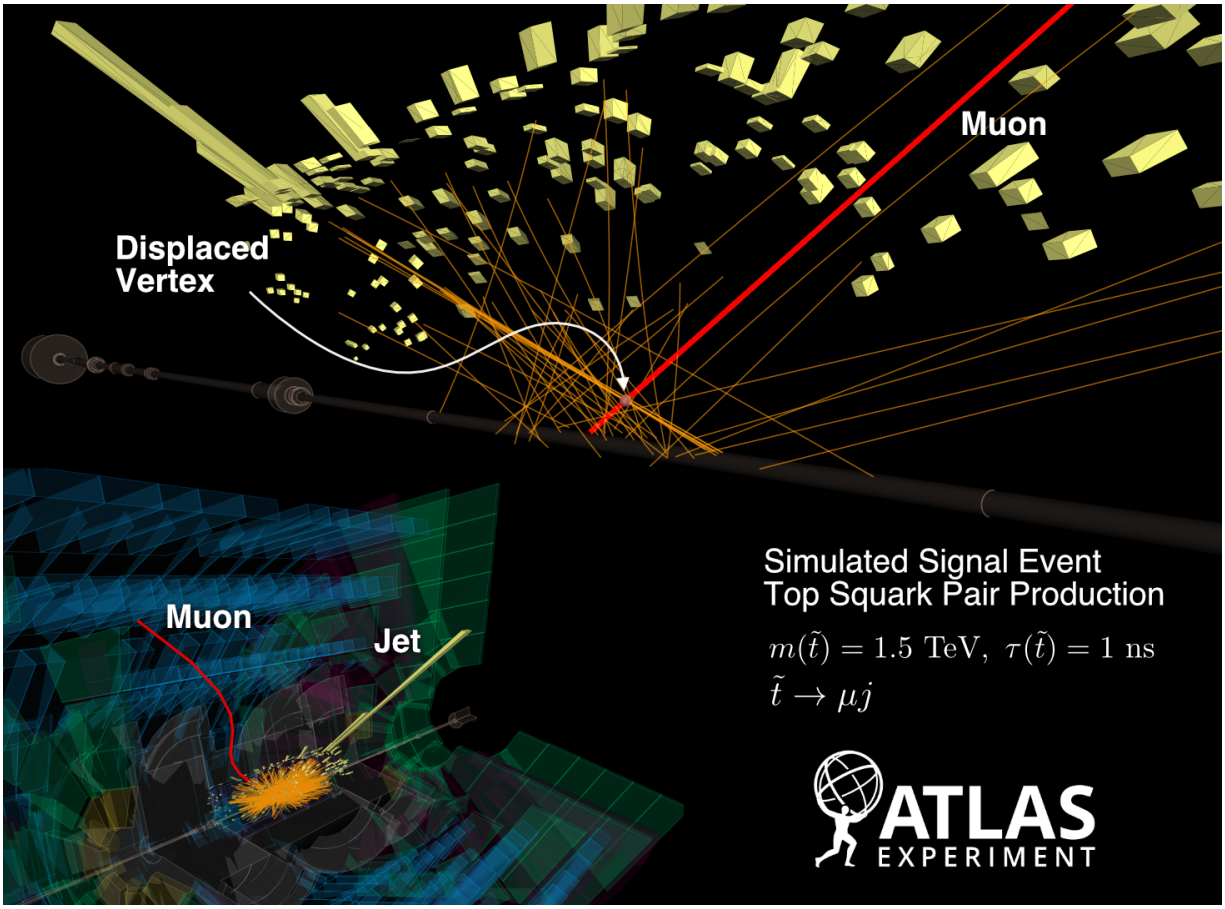

Figure 6: An event display of a simulated signal event is showing the decay of one top squark $\tilde{t}$ to a muon and a hadronic jet. Clusters of energy in the calorimeter are shown as yellow boxes. A selection of Inner Detector tracks are shown in orange. A reconstructed displaced vertex is shown as a red sphere. The red line denotes a reconstructed muon track.

Appendix

A Event displays

Event displays are shown for a simulated signal event (Figure 6) and the data candidate event (Figure 7).

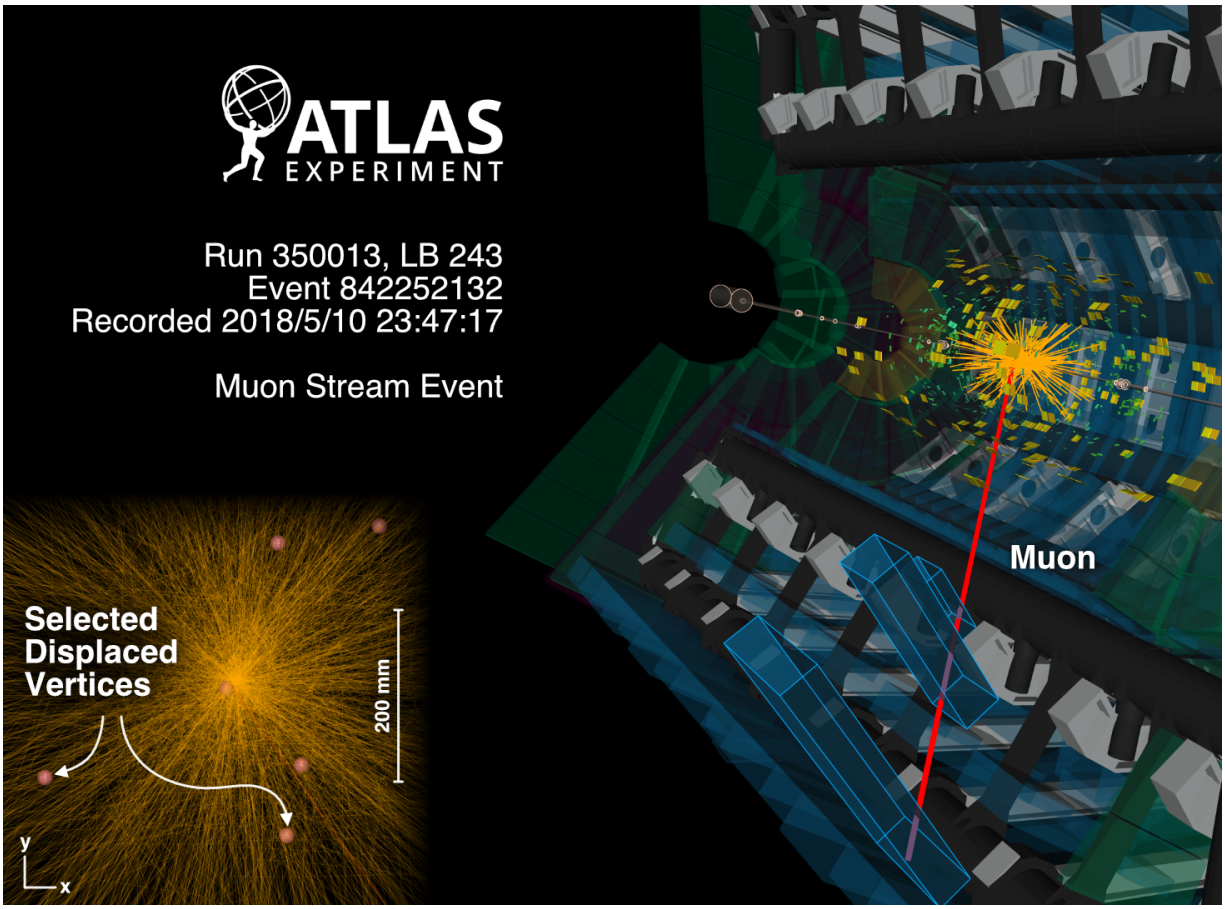

Figure 7: An event display of the one event that satisfies the Muon Stream signal region requirements. Clusters of energy in the calorimeter are shown as yellow boxes. A selection of Inner Detector tracks are shown in orange. Reconstructed displaced vertices are shown as red spheres. The red line denotes a reconstructed muon track.

References

[1] R. Barbieri and G. F. Giudice, *Upper Bounds on Supersymmetric Particle Masses*, Nucl. Phys. B **306** (1988) 63.

[2] B. de Carlos and J. A. Casas, *One loop analysis of the electroweak breaking in supersymmetric models and the fine tuning problem*, Phys. Lett. B **309** (1993) 320, arXiv: hep-ph/9303291.

[3] G. Bertone, D. Hooper, and J. Silk, *Particle dark matter: Evidence, candidates and constraints*, Phys. Rept. **405** (2005) 279, arXiv: hep-ph/0404175 [hep-ph].

[4] M. Fairbairn, A. C. Kraan, D. A. Milstead, T. Sjostrand, P. Z. Skands and T. Sloan, *Stable massive particles at colliders*, Phys. Rept. **438** (2007), arXiv: 0611040 [hep-ph].

[5] L. Lee, C. Ohm, A. Soffer, and T.-T. Yu, *Collider searches for long-lived particles beyond the Standard Model*, Progress in Particle and Nuclear Physics **3695** (2019), arXiv: 1810.12602.

[6] Y. A. Golfand and E. P. Likhtman, *Extension of the Algebra of Poincare Group Generators and Violation of p Invariance*, JETP Lett. **13** (1971) 323, [Pisma Zh. Eksp. Teor. Fiz. **13** (1971) 452].

[7] D. V. Volkov and V. P. Akulov, *Is the Neutrino a Goldstone Particle?*, Phys. Lett. B **46** (1973) 109.

[8] J. Wess and B. Zumino, *Supergauge Transformations in Four-Dimensions*, Nucl. Phys. B **70** (1974) 39.

[9] J. Wess and B. Zumino, *Supergauge Invariant Extension of Quantum Electrodynamics*, Nucl. Phys. B **78** (1974) 1.

[10] S. Ferrara and B. Zumino, *Supergauge Invariant Yang-Mills Theories*, Nucl. Phys. B **79** (1974) 413.

[11] A. Salam and J. A. Strathdee, *Supersymmetry and Nonabelian Gauges*, Phys. Lett. B **51** (1974) 353.

[12] N. Sakai, *Naturalness in Supersymmetric Guts*, Z. Phys. C **11** (1981) 153.

[13] S. Dimopoulos, S. Raby, and F. Wilczek, *Supersymmetry and the Scale of Unification*, Phys. Rev. D **24** (1981) 1681.

[14] L. E. Ibanez and G. G. Ross, *Low-Energy Predictions in Supersymmetric Grand Unified Theories*, Phys. Lett. B **105** (1981) 439.

[15] S. Dimopoulos and H. Georgi, *Softly Broken Supersymmetry and SU(5)*, Nucl. Phys. B **193** (1981) 150.

[16] K. Inoue, A. Kakuto, H. Komatsu, and S. Takeshita, *Aspects of Grand Unified Models with Softly Broken Supersymmetry*, Prog. Theor. Phys. **68** (1982) 927.

[17] J. R. Ellis and S. Rudaz, *Search for Supersymmetry in Toponium Decays*, Phys. Lett. B **128** (1983) 248.

[18] G. 't Hooft, *Computation of the Quantum Effects Due to a Four-Dimensional Pseudoparticle*, Phys. Rev. **D14** (1976) 3432.

[19] V. A. Kuzmin, V. A. Rubakov, and M. E. Shaposhnikov, *On the Anomalous Electroweak Baryon Number Nonconservation in the Early Universe*, Phys. Lett. **155B** (1985) 36.

[20] P. Fayet, *Supersymmetry and Weak, Electromagnetic and Strong Interactions*, Phys. Lett. B **64** (1976) 159.

[21] P. Fayet, *Spontaneously Broken Supersymmetric Theories of Weak, Electromagnetic and Strong Interactions*, Phys. Lett. B **69** (1977) 489.

[22] G. R. Farrar and P. Fayet, *Phenomenology of the Production, Decay, and Detection of New Hadronic States Associated with Supersymmetry*, Phys. Lett. B **76** (1978) 575.

[23] H. Goldberg, *Constraint on the Photino Mass from Cosmology*, Phys. Rev. Lett. **50** (1983) 1419.

[24] J. R. Ellis, J. S. Hagelin, D. V. Nanopoulos, K. A. Olive, and M. Srednicki, *Supersymmetric Relics from the Big Bang*, Nucl. Phys. B **238** (1984) 453.

[25] R. Barbier et al., *R-parity violating supersymmetry*, Phys. Rept. **420** (2005) 1, arXiv: hep-ph/0406039 [hep-ph].

[26] C. Friberg, E. Norrbin, and T. Sjostrand, *QCD aspects of leptoquark production at HERA*, Phys. Lett. B **403** (1997) 329, arXiv: hep-ph/9704214 [hep-ph].

[27] M. J. Strassler and K. M. Zurek, *Discovering the Higgs through highly-displaced vertices*, Phys. Lett. B **661** (2008) 263, arXiv: hep-ph/0605193 [hep-ph].

[28] Y. Cui and B. Shuve, *Probing Baryogenesis with Displaced Vertices at the LHC*, JHEP **02** (2015) 049, arXiv: 1409.6729 [hep-ph].

[29] T. Asaka and M. Shaposhnikov, *The nuMSM, dark matter and baryon asymmetry of the universe*, Phys. Lett. B **620** (2005) 17, arXiv: hep-ph/0505013 [hep-ph].

[30] B. C. Allanach, M. A. Bernhardt, H. K. Dreiner, C. H. Kom, and P. Richardson, *Mass Spectrum in R-Parity Violating mSUGRA and Benchmark Points*, Phys. Rev. D **75** (2007) 035002, arXiv: hep-ph/0609263 [hep-ph].

[31] ATLAS Collaboration, *Search for B-L R-parity-violating top squarks in $\sqrt{s}$=13 TeV pp collisions with the ATLAS experiment*, Phys. Rev. D **97** (2018) 032003, arXiv: 1710.05544 [hep-ex].

[32] CMS Collaboration, *Search for pair production of second-generation leptoquarks at $\sqrt{s}$ = 13 TeV*, Phys. Rev. D **99** (2019), arXiv: 1808.05082 [hep-ex].

[33] CMS Collaboration, *Search for new long-lived particles at $\sqrt{s}$ = 13 TeV*, Phys. Lett. B **780** (2018) 432, arXiv: 1711.09120 [hep-ex].

[34] CMS Collaboration, *Search for Displaced Supersymmetry in events with an electron and a muon with large impact parameters*, Phys. Rev. Lett. **114** (2015) 061801, arXiv: 1409.4789 [hep-ex].

[35] CMS Collaboration, *Search for long-lived particles decaying into displaced jets in proton-proton collisions at $\sqrt{s}$ = 13 TeV*, Phys. Rev. D **99** (2019) 032011, arXiv: 1811.07991 [hep-ex].

[36] ATLAS Collaboration, *Search for displaced vertices arising from decays of new heavy particles in 7 TeV pp collisions at ATLAS*, Phys. Lett. B **707** (2012) 478, arXiv: 1109.2242 [hep-ex].

[37] ATLAS Collaboration, *Search for long-lived, heavy particles in final states with a muon and multi-track displaced vertex in proton-proton collisions at $\sqrt{s}$ = 7 TeV with the ATLAS detector*, Phys. Lett. B **719** (2013) 280, arXiv: 1210.7451 [hep-ex].

[38] ATLAS Collaboration, *The ATLAS Experiment at the CERN Large Hadron Collider*, JINST **3** (2008) S08003.

[39] ATLAS Collaboration, *ATLAS Insertable B-Layer Technical Design Report*, ATLAS-TDR-19, 2010, URL: https://cds.cern.ch/record/1291633, *ATLAS Insertable B-Layer Technical Design Report Addendum*, ATLAS-TDR-19-ADD-1, 2012, URL: https://cds.cern.ch/record/1451888.

[40] ATLAS Collaboration, *Performance of the ATLAS trigger system in 2015*, Eur. Phys. J. C **77** (2017) 317, arXiv: 1611.09661 [hep-ex].

[41] G. Avoni et al., *The new LUCID-2 detector for luminosity measurement and monitoring in ATLAS*, JINST **13** (2018) P07017.

[42] ATLAS Collaboration, *Luminosity determination in pp collisions at $\sqrt{s}$ = 8 TeV using the ATLAS detector at the LHC*, Eur. Phys. J. C **76** (2016) 653, arXiv: 1608.03953 [hep-ex].

[43] J. Alwall, R. Frederix, S. Frixione, V. Hirschi, F. Maltoni, et al., *The automated computation of tree-level and next-to-leading order differential cross sections, and their matching to parton shower simulations*, JHEP **07** (2014) 079, arXiv: 1405.0301 [hep-ph].

[44] T. Sjöstrand et al., *An Introduction to PYTHIA 8.2*, Comput. Phys. Commun. **191** (2015) 159, arXiv: 1410.3012 [hep-ph].

[45] ATLAS Collaboration, *ATLAS Pythia 8 tunes to 7 TeV data*, ATL-PHYS-PUB-2014-021, 2014, URL: https://cds.cern.ch/record/1966419.

[46] R. D. Ball et al., *Parton distributions with LHC data*, Nucl. Phys. B **867** (2013) 244, arXiv: 1207.1303 [hep-ph].

[47] ATLAS Collaboration, *The ATLAS Simulation Infrastructure*, Eur. Phys. J. C **70** (2010) 823, arXiv: 1005.4568 [physics.ins-det].

[48] S. Agostinelli et al., *GEANT4: A Simulation toolkit*, Nucl. Instrum. Meth. A **506** (2003) 250.

[49] A. C. Kraan, *Interactions of heavy stable hadronizing particles*, Eur. Phys. J. C **37** (2004) 91, arXiv: hep-ex/0404001.

[50] R. Mackeprang and A. Rizzi, *Interactions of Coloured Heavy Stable Particles in Matter*, Eur. Phys. J. C **50** (2007) 353, arXiv: hep-ph/0612161.

[51] R. Mackeprang and D. Milstead, *An Updated Description of Heavy-Hadron Interactions in GEANT-4*, Eur. Phys. J. C **66** (2010) 493, arXiv: 0908.1868 [hep-ph].

[52] W. Beenakker, C. Borschensky, M. Krämer, A. Kulesza, and E. Laenen, *NNLL-fast: predictions for coloured supersymmetric particle production at the LHC with threshold and Coulomb resummation*, JHEP **12** (2016) 133, arXiv: 1607.07741 [hep-ph].

[53] W. Beenakker, M. Krämer, T. Plehn, M. Spira, and P. M. Zerwas, *Stop production at hadron colliders*, Nucl. Phys. B **515** (1998) 3, arXiv: hep-ph/9710451.

[54] W. Beenakker et al., *Supersymmetric top and bottom squark production at hadron colliders*, JHEP **08** (2010) 098, arXiv: 1006.4771 [hep-ph].

[55] W. Beenakker et al., *NNLL resummation for stop pair-production at the LHC*, JHEP **05** (2016) 153, arXiv: 1601.02954 [hep-ph].

[56] J. Butterworth et al., *PDF4LHC recommendations for LHC Run II*, J. Phys. G **43** (2016) 023001, arXiv: 1510.03865 [hep-ph].

[57] P. Nason, *A new method for combining NLO QCD with shower Monte Carlo algorithms*, JHEP **11** (2004) 040, arXiv: hep-ph/0409146.

[58] ATLAS Collaboration, *Performance of the reconstruction of large impact parameter tracks in the inner detector of ATLAS*, ATL-PHYS-PUB-2017-014, 2017, URL: https://cds.cern.ch/record/2275635.

[59] ATLAS Collaboration, *Jet energy measurement with the ATLAS detector in proton–proton collisions at $\sqrt{s}$ = 7 TeV*, Eur. Phys. J. C **73** (2013) 2304, arXiv: 1112.6426 [hep-ex].

[60] ATLAS Collaboration, *Jet energy scale measurements and their systematic uncertainties in proton–proton collisions at $\sqrt{s}$ = 13 TeV with the ATLAS detector*, Phys. Rev. D **96** (2017) 072002, arXiv: 1703.09665 [hep-ex].

[61] M. Baak et al., *HistFitter software framework for statistical data analysis*, Eur. Phys. J. C **75** (2015) 153, arXiv: 1410.1280 [hep-ex].

[62] A. L. Read, *Presentation of search results: the CL_S technique*, J. Phys. G **28** (2002) 2693.